Title

Strongly coupled intermediate electronic states in one-color two-photon single valence ionization of O2

Journal

The Journal of Chemical Physics, 158(2)

ISSN

0021-9606

Authors

Larsen, Kirk A
Bello, Roger Y
Lucchese, Robert R
et al.

Publication Date

2023-01-14

DOI

10.1063/5.0128846

Peer reviewed

Strongly coupled intermediate electronic states in one-color two-photon single valence ionization of O_2

Kirk A. Larsen,[1,2,3,a)] Roger Y. Bello,[2,4,b)] Robert R. Lucchese,[2] C. William McCurdy,[2,5] Daniel S. Slaughter,[2] and Thorsten Weber[2,c)]

[1)] *Graduate Group in Applied Science and Technology, University of California, Berkeley, CA 94720, USA*

[2)] *Chemical Sciences Division, Lawrence Berkeley National Laboratory, Berkeley, CA 94720, USA*

[3)] *Stanford PULSE Institute, SLAC National Accelerator Laboratory, Menlo Park, California 94025, USA*

[4)] *Departamento de Química, Módulo 13, Universidad Autónoma de Madrid, 28049 Madrid, Spain*

[5)] *Department of Chemistry, University of California, Davis, CA 95616, USA*

(Dated: 1 December 2022)

We present an experimental and theoretical energy- and angle-resolved investigation on the non-dissociative photoionization dynamics of near-resonant one-color two-photon single valence ionization of neutral O_2 molecules. Using 9.3 eV femtosecond pulses produced via high harmonic generation and a 3-D momentum imaging spectrometer, we detect the photoelectrons and O_2^+ cations produced from one-color two-photon ionization in coincidence. The measured and calculated photoelectron angular distributions show agreement, which indicates that a superposition of two intermediate electronic states is dominantly involved and that wavepacket motion on those near-resonantly populated intermediate states does not play a significant role in the measured two-photon ionization dynamics. Here we find greater utility in the diabatic representation compared to the adiabatic representation, where invoking a single valence-character diabat is sufficient to describe the underlying two-photon ionization mechanism.

PACS numbers: Valid PACS appear here

I. INTRODUCTION

Two-photon ionization of atomic and molecular systems can be accurately described within the framework of second order perturbation theory, involving a summation over intermediate electronic states[1–6]. Depending on the photon energy, the number of intermediate states that must be included to capture the photoionization dynamics varies. In general, as the photon energy is detuned from intermediate electronic states, the non-resonant contribution to the two-photon ionization dynamics increases, where more intermediate states must be included to provide an adequate description of the photoionization. As the photon energy is tuned closer to intermediate electronic states, the terms in the summation belonging to those intermediates begin to dominate. In this case, the non-resonant contribution decreases, and the sum can be truncated to only include a small number of resonant or near-resonant terms. In nonlinear optics, with the proliferation of high-intensity vacuum ultraviolet (VUV) sources, it remains to be established to what degree the non-resonant terms contribute in resonant (or near-resonant) two-photon ionization processes.

In diatomic molecules, the eigenvalues of the Hamiltonian cannot become degenerate with varying bond length, which results in avoided crossings of electronic states. In the vicinity of an avoided crossing, the energetic spacing between the two eigenvalues becomes small, allowing a superposition of the two corresponding eigenstates to be excited with a relatively narrow-band laser pulse. The $B^3\Sigma_u^-$ and $E^3\Sigma_u^-$ states of molecular oxygen are well-known to be mixed states due to the interaction between the valence and Rydberg configurations of the two electronic states[7–16]. Their adiabatic potential energy curves exhibit an avoided crossing ∼9.5 eV above the ground electronic state in the Franck-Condon region. For near-resonant photoexcitation at energies approaching the energy of the avoided crossing, a superposition of these two electronic states is created. This superposition can then be probed by photoionization, which projects the excited wavepacket to a set of continuum electronic states. A sensitive observable is the photoelectron angular distribution, the shape of which reveals information on the relative contribution of each state, which depends on the electronic state symmetries and character, the dipole coupling strengths, and the internuclear distance between the atoms in the molecule.

In this work we present experimental and theoretical results on energy- and angle-resolved near-resonant one-color two-photon single ionization of molecular oxygen using 3-D momentum imaging. In this non-dissociative ionization process the photoelectron and molecular cation are measured in coincidence. Using a 400 nm driving field, we produce and select femtosecond

[a)] Electronic mail: larsenk@stanford.edu
[b)] Electronic mail: roger.bello@uam.es
[c)] Electronic mail: TWeber@lbl.gov

VUV pulses with an energy of 9.3 eV via High Harmonic Generation (HHG). These high-intensity VUV pulses, which are near-resonant with the $B^3\Sigma_u^-$ and $E^3\Sigma_u^-$ states, are used to singly ionize the molecular oxygen target via two-photon ionization.

We find that a superposition of the $B^3\Sigma_u^-$ and $E^3\Sigma_u^-$ electronic states is generated in the first photoabsorption step, where the contribution from each state varies with internuclear separation in a way that creates a valence-character wavepacket at equilibrium R and larger bond lengths as the wavepacket spreads and dissociates. This allows both non-resonant terms in the perturbation theory expansion and wavepacket motion to be neglected in the calculations, while still accurately reproducing the measured two-photon ionization dynamics. We show that this can be explained within the diabatic representation constructed from the $B^3\Sigma_u^-$ and $E^3\Sigma_u^-$ adiabatic states, and demonstrate that although our measurement exhibits some sensitivity to motion on the intermediate states, we primarily probe early time dynamics in the vicinity of an avoided crossing, before the wavepacket has spread or moved out of the Franck-Condon region significantly.

II. EXPERIMENT

The experimental set-up and conditions are similar to those described in[17], thus only a brief description is provided below. The valence photoionization dynamics in neutral O_2 were investigated using the COLd Target Recoil Ion Momentum Spectroscopy (COLTRIMS) technique[18–21], where the photoelectrons and bound O_2^+ cations produced by one-color two-photon single ionization are collected with full 4π solid angle. The 3-D momenta of the charged particles are measured in coincidence on an event-by-event basis. The electrons and ions are guided by parallel DC electric and magnetic fields (12.26 V/cm, 4.55 G) towards their respective position- and time-sensitive detectors at opposite ends of the 3-D momentum imaging spectrometer. The detectors consist of a Multi-Channel Plate (MCP) stack in chevron configuration with a delay-line anode readout[22]. The electron and ion detectors are a three layer hex-anode with a 80 mm MCP stack and a two layer quad-anode with a 120 mm MCP stack, respectively. Here a charge carrier's 3-D momentum is encoded into its hit position on the detector and its time-of-flight relative to the laser trigger. In this configuration, the energy resolution of the spectrometer for the electrons is roughly 1:10 (i.e. at 5 eV of kinetic energy, we have approximately 500 meV resolution).

Near-infrared (NIR) laser pulses (12 mJ, 45 femtoseconds, 800 nm) from a 50 Hz Ti:sapphire laser system are frequency doubled using a 0.25 mm thick beta-barium borate (BBO) crystal, where the copropagating NIR and blue fields are then separated using two dichroic mirrors. The reflected 400 nm photons (∼3.6 mJ, ∼50 fs) are used to generate femtosecond VUV pulses via HHG, by loosely focusing (f = 6 m) the 400 nm pulses into a 10 cm long gas cell containing 2 Torr of krypton. The resulting VUV frequency comb is then separated from the 400 nm driving field by reflection from three Si mirrors near Brewster's angle for the blue light, resulting in a suppression of the driving field by a factor of $< 10^{-6}$. The 3$^{\text{rd}}$ harmonic (133 nm, 9.3 eV) is selected via transmission through a 0.30 mm thick MgF_2 VUV bandpass filter (Acton Optics FB130-B-1D.3), which totally suppresses the 5$^{\text{th}}$ harmonic and above. The femtosecond pulse duration of the 3$^{\text{rd}}$ harmonic is also maintained, while temporally separating the residual fundamental pulse from the 3$^{\text{rd}}$ harmonic pulse by roughly 850 fs, due to the difference in the group velocity dispersion (GVD) of the window at ω_0 and $3\omega_0$[23,24]. After transmission through the window, we estimate the pulse duration of the 3$^{\text{rd}}$ harmonic to be ∼35-40 fs, based on its spectral bandwidth, its estimated attochirp, and the thickness and GVD of the MgF_2 window[25,26]. The femtosecond 9.3 eV pulses are then back-focused (f = 15 cm) into the 3-D momentum imaging spectrometer using a protected Al mirror. The reflectance of this back-focusing mirror has been measured to be 43% at 9.3 eV[27]. The pulse energy of the 3$^{\text{rd}}$ harmonic on target is approximately 10 nJ, which was measured using a pair of bandpass VUV filters (same as above) and a calibrated photodiode. At this pulse energy and focal length, the field strength is perturbative, such that no three-photon transitions (or higher order), or strong-field processes were observed. From a previous measurement on argon[28], the VUV spectrum of the 9.3 eV femtosecond pulse is known to be roughly Gaussian in shape and possesses no sidebands or pedestal, characteristic of the VUV frequency combs generated in the single-color HHG, with a two-photon bandwidth of ∼300 meV.

A rotationally and vibrationally cold beam of oxygen molecules (approximately 80 K) is prepared via an adiabatic expansion through a 0.03 mm nozzle. The emerging gas jet is then collimated by a pair of skimmers. This molecular jet propagates perpendicular to the focused VUV beam, where the two intersect in the interaction region of the spectrometer (∼0.01 × 0.01 × 0.20 mm), resulting in a measured two-photon ionization rate of approximately 20 Hz by two-photon absorption in the target oxygen molecules. No significant ionization processes due to gas impurities or higher photon energies were observed.

III. THEORY

The photoelectron angular distributions for two-photon ionization of O_2 were computed using second order time-independent perturbation theory[29–33] for the

two-photon absorption amplitude in the form

$$J_{fi} = (\hbar\omega)^2 \sum_j \frac{\langle\Psi_f|\hat{n}\cdot\vec{r}|\Psi_j\rangle\langle\Psi_j|\hat{n}\cdot\vec{r}|\Psi_i\rangle}{\Delta E_{j,i} - \hbar\omega} \qquad (1)$$

in which the factor of $(\hbar\omega)^2$ arises from manipulations to give a length form in better agreement with the velocity form when the intermediate states included do not form a complete set[34]. In Eq.(1) $\Psi_{i,f}$ denotes the initial (bound) and final (continuum) states, $\Delta E_{j,i} = E_j - E_i$, and $\hat{n}$ is the polarization vector of both photons.

Explicit expressions for the β_2 and β_4 parameters used in the parametrization of the photoelectron angular distributions can be derived from Eq.(1). Our calculations of the angular distributions for various final states were performed at a single internuclear distance, but the choice of intermediate states requires an understanding of both the potential energy curves for the intermediate states and the behavior with varying internuclear distance of the dipole couplings in Eq.(1).

The potential energy curves and dipole couplings between neutral O_2 states were computed using the multireference configuration interaction capability of MOLPRO[35,36], with singles and doubles excitations from an active space including four σ_g, four σ_u, and both components of two π_u and one π_g orbitals, with the $1\sigma_g$ and $1\sigma_u$ core orbitals always doubly occupied. These orbitals were obtained from a state-averaged complete active space self-consistent field (CAS-SCF) calculation, including one $^3\Sigma_g^-$, two $^3\Sigma_u^-$, two $^3\Delta_u$ and two $^3\Pi_u$ states. The one-electron basis set was aug-cc-pVTZ[37,38], augmented by five s, five p, and five d Rydberg diffuse functions[39] centered at the bond midpoint.

Dipole couplings and potential energy curves for dipole allowed states near resonance for a photon energy of 9.3 eV are shown in Fig. 1. The apparent discontinuity observed near $R = 2.8a_0$ is due to the nature of the calculation and results from switching from occupied to virtual orbitals in the CAS-SCF approach used. The four states shown there undergo widely avoided crossings that in both cases ($B\,^3\Sigma_u^-$ with $E\,^3\Sigma_u^-$ and $a\,^3\Pi_u$ with $F\,^3\Pi_u$) involve a change between valence and Rydberg character in these adiabatic states. To understand the behavior of the transition dipole moments in Fig. 1(b), it is useful to think in terms of the diabatic representation of these states. For example, near their avoided crossing the E and B states are given by a unitary transformation,

$$\begin{pmatrix}|\psi_B(R)\rangle\\|\psi_E(R)\rangle\end{pmatrix} = \begin{pmatrix}b_1(R) & b_2(R)\\e_1(R) & e_2(R)\end{pmatrix}\begin{pmatrix}|\phi_{\rm val}\rangle\\|\phi_{\rm Ryd}\rangle\end{pmatrix}, \qquad (2)$$

of valence and Rydberg diabatic states $|\phi_{val}\rangle$ and $|\phi_{Ryd}\rangle$. On the small R side of the avoided crossing in Fig. 1(a), the E state is predominantly valence-like while on the large R side the B state acquires valence character. The valence diabatic state has a much larger transition dipole moment with the ground state than the Rydberg diabatic state, and Fig. 1(b) displays the effect of the changing

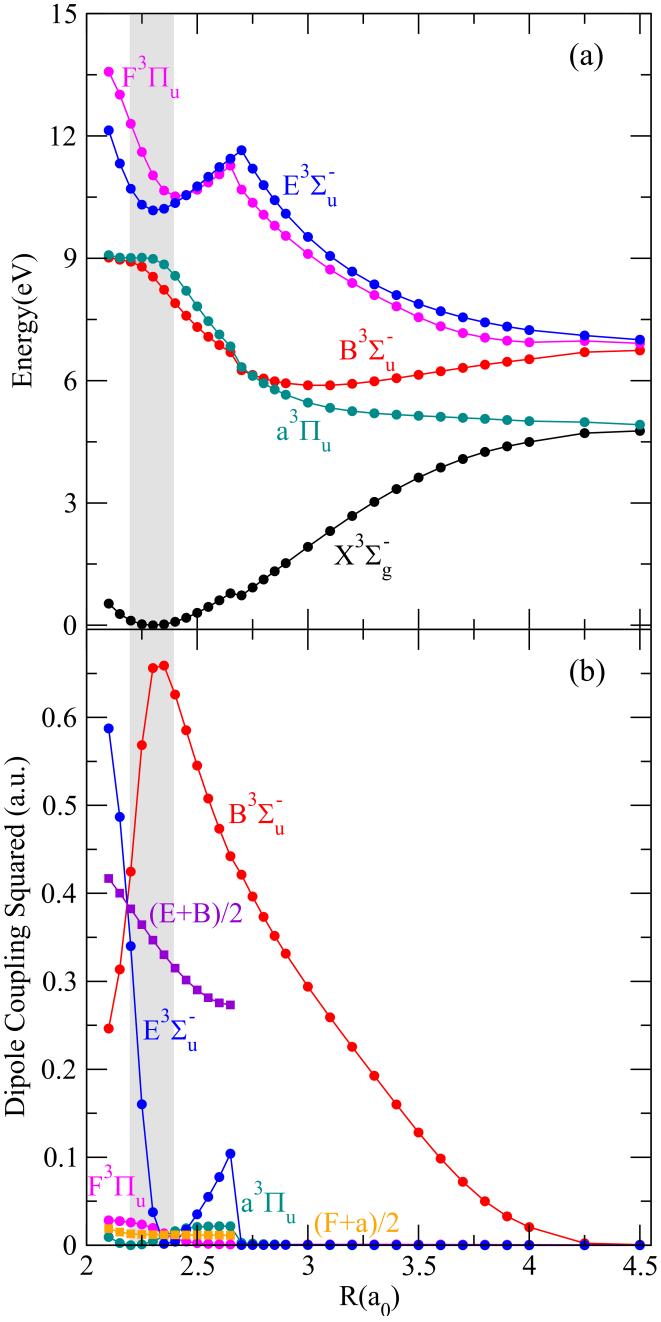

FIG. 1. (a) Relevant potential energy curves of O_2. (b) Squares of the transition dipole moments with the ground state for each of the excited states in the first photoexcitation step. The shaded interval shown in (a) and (b) indicates the Franck-Condon region. Note that the discontinuity at R=2.8 a$_0$, particularly seen in the $E\,^3\Sigma_u^-$ and $F\,^3\Pi_u$ states, is caused by a switching between occupied and virtual orbitals in the limited CAS-SCF calculation used here.

character of these two states. The unitarity of the transformation between diabatic and adiabatic states (requiring $b_1^2 + e_1^2 = 1$) is reflected by the fact that the sum of the computed transition moments of the B and E states

is roughly constant with changing R in crossing region (shown as the purple curve). The same can be seen in Fig. 1(b) to be true for the case of the a and F states (shown as the gold curve).

Moreover, parallel excitations into the $B^3\Sigma_u^-$ and $E^3\Sigma_u^-$ states are more than an order of magnitude larger than those for the $a^3\Pi_u$ and $F^3\Pi_u$ at the equilibrium internuclear distance. Thus, at these photon energies ($\hbar\omega \approx 9.3$ eV) parallel dipole transitions to the nearby states are favored over perpendicular transitions, while the second photon transition may be either parallel or perpendicular, leading to ${}^3\Sigma_g^-$ and ${}^3\Pi_g$ final symmetries. For these reasons, it turns out to be a reasonable first approximation to include only the $B\,{}^3\Sigma_u^-$ and $E\,{}^3\Sigma_u^-$ intermediate states in the sum in Eq.(1).

With that approximation two-photon single ionization β_2 and β_4 anisotropy parameters were calculated at a fixed internuclear distance of R=2.30 a_0 (bohr). The calculations have been performed considering randomly oriented molecules, because the two-photon energy lies below the dissociative ionization threshold, preventing the molecular orientation at the instant of photoionization from being determined without prealignment.

Dipole couplings between the excited neutral intermediate states and the scattering states require a coupled channel treatment of the ionization continuum in this case. The scattering states were calculated using the Schwinger variational method[40–43]. In these calculations, the scattering-states at a fixed energy were represented on single center expanded grid, with a partial wave expansion up to $l_{\max}$=80. The full N-electron ionized state was then represented as a close-coupling expansion containing a sum of the products of $(N-1)$-electron ion state wave functions multiplied with one-electron photoelectron wave functions. The ion channels in the close-coupling expansion included $X^2\Pi_g$, $a^4\Pi_u$, $A^2\Pi_u$, $b^4\Sigma_g^-$, $B^2\Sigma_g^-$, $1^4\Pi_g$, $3^2\Pi_u$, and $c^4\Sigma_u^-$ states. The ionization potentials for each of these channels were shifted slightly to agree with the experimental vertical ionization potentials in Refs.[44,45]. The initial and ion states were computed performing a numerical complete active space configuration interaction (CAS-CI) method using the orbitals from the CAS-SCF calculation discussed above, where spin-orbit interaction has been ignored.

IV. RESULTS

The photoelectron kinetic energy spectrum for electrons measured in coincidence with the O_2^+ cation is shown in Fig. 2 as a histrogram. The measured distribution exhibits a large and broad peak near 0 eV that is associated with the $a^4\Pi_u$, $A^2\Pi_u$, and $b^4\Sigma_g^-$ ionic states of O_2, and a smaller peak near 6.25 eV that is associated with the $X^2\Pi_g$ ionic state of O_2. The branching ratio of the high and low kinetic energy features is approximately 1:4, where 4.2 eV is taken as the energy separating the two features. The larger signal amplitude at low kinetic

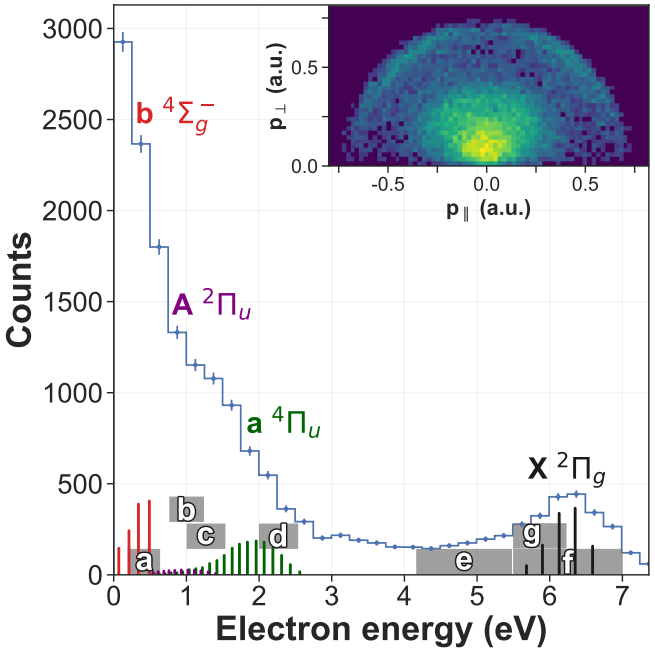

FIG. 2. The measured photoelectron kinetic energy spectrum for near-resonant one-color two-photon single ionization of O_2. The lettered gray horizontal bars indicate different energy intervals corresponding to the various ionic states that are subsequently analyzed and shown in Fig. 3 and Table I. The vertical colored lines indicate the location of the vibrational levels of the various ionic states and the corresponding Franck-Condon factors reported in[45]. (Inset) The photoelectron momentum distribution parallel and perpendicular to the VUV polarization.

energy can be attributed to the fact that the two-photon energy is closer to resonance with the higher lying ionic states, leading to an increased propensity to ionize to excited ionic states over the ground ionic state. The vibrational levels associated with these different electronic states of the O_2^+ cation and their corresponding Franck-Condon factors (scaled for visibility) with the ground state of neutral O_2 are indicated by the color-coded vertical line segments[45]. The vibrational states associated with the $A^2\Pi_u$ ionic state overlap in energy with those of the adjacent $a^4\Pi_u$, while those associated with the $b^4\Sigma_g^-$ state can be separated in energy. Given the two-photon excitation energy and bandwidth (∼18.6 eV and ∼300 meV, respectively), the widths of the features in Fig. 2 are primarily determined by the electron energy resolution of our spectrometer (∼500 meV) and the spectral bandwidth of the VUV pulse, which exceeds the indicated vibrational level spacing (see colored vertical lines). The excitation bandwidth and spectrometer resolution results in the unresolved broad low energy feature corresponding to the $a^4\Pi_u$, $A^2\Pi_u$, and $b^4\Sigma_g^-$ ionic states and the unresolved vibrational progressions for all four ionic states. We observe that in the case of the $X^2\Pi_g$ state (the high kinetic energy feature), the general shape of

the two-photon electron kinetic energy spectrum bares close resemblance to the one-photon Franck-Condon factors, which we will address in more detail below.

The features in the photoelectron spectrum are partitioned into different regions, with the lettered grey horizontal bars in Fig. 2 indicating different intervals of electron kinetic energy that are subsequently analyzed. These energy slices sum over two or more vibrational levels, as the two-photon bandwidth, energy resolution, and statistics do not permit a fully vibrationally resolved measurement. The broad low kinetic energy feature is divided into four regions, 0.25–0.60 eV, 0.80–1.20 eV, 1.00–1.50 eV and 2.00–2.50 eV, where the lowest energy slice primarily captures the $b^4\Sigma_g^-$ ionic state, the two intermediate energy slices primarily capture the $A^2\Pi_u$ and the higher energy slice primarily captures the $a^4\Pi_u$ ionic state. Although the vibrational levels of both the $A^2\Pi_u$ and $a^4\Pi_u$ states overlap over the two intermediate energy intervals, calculated partial-photoionization cross sections (not shown here) indicate a dominance of the $A^2\Pi_u$ channel over the $a^4\Pi_u$ channel in this energy region. The high kinetic energy feature, associated with the $X^2\Pi_g$ ionic state, is divided into two regions, 5.50–6.20 eV and 5.50–7.00 eV. We additionally analyze photoelectrons emerging from the 4.20–5.50 eV kinetic energy region, which does not overlap with any of the Franck-Condon factors. These photoelectrons result from wavepacket motion and dissociation on the intermediate electronic states preceding ionization to the $X^2\Pi_g$ state of the cation, which leads to an increased binding energy (i.e. a lower photoelectron kinetic energy).

The photoelectron momentum distribution for the transverse and parallel momentum components with respect to the VUV polarization vector is shown in the inset of Fig. 2. Here we see an outer anisotropic arc feature possessing higher photoelectron momentum, which is associated with the $X^2\Pi_g$ ionic state, and two inner anisotropic arc features at lower photoelectron momentum associated with the $A^2\Pi_u$, $a^4\Pi_u$, and $b^4\Sigma_g^-$ ionic states. To gain deeper insight into the anisotropy of the photoelectron emission patterns for each of these ionic states, we turn to the energy- and angle-differential photoionization cross sections. For a two-photon ionization process, the energy-dependent and angle-differential photoionization cross section of a target molecule by linearly polarized light is given by:

$$\frac{d^2\sigma}{d\Omega dE} = \frac{\sigma_0(E)}{4\pi}\left[1 + \beta_2(E)P_2(\cos\theta) + \beta_4(E)P_4(\cos\theta)\right], \tag{3}$$

where σ_0 is the total photoionization cross section, θ is the angle between the photoelectron momentum vector and the polarization vector ϵ of the light, E is the photoelectron kinetic energy, β_2, β_4 are the second and fourth order anisotropy parameters, and P_2 and P_4 are the second and fourth order Legendre polynomials with the argument $\cos\theta$.

The measured (solid red circles with error bars), calculated (red lines), and fitted (blue lines) photoelectron angular distributions for each of the energy regions highlighted in Fig. 2 are presented in Fig. 3. The corresponding β parameters can be found in Table I. The error bars in Fig. 3 and the experimental errors quoted in Table I represent ± 1 standard deviation. The error on the β parameters was determined via statistical bootstrapping[46].

The angular distribution for the 0.25–0.60 eV kinetic energy interval, associated with the $b^4\Sigma_g^-$ ionic state, is presented in panel (a) of Fig. 3. In this case the angular distribution exhibits a nearly isotropic emission pattern, with shallow minima around $\pi/4$ and $3\pi/4$. As the electron energy is very low, only the lower order partial waves are important, resulting in a nearly isotropic angular distribution, with a slight enhancement along the VUV polarization vector, captured by the small positive value of β_2 and near-zero value of β_4 seen in Table I.

The photoelectron angular distributions for the 0.80–1.20 eV and 1.00–1.50 eV kinetic energy intervals, associated with the $A^2\Pi_u$ ionic state, are presented in panels (b) and (c) of Fig. 3, respectively. The photoelectron emission patterns have attributes associated with a d-wave, but appear more isotropic, showing shallow minima at 0, $\pi/2$, and π. This is also indicated by the small values of β_2 and small negative values of β_4 shown in Table I.

The angular distribution for the 2.00–2.50 eV kinetic energy interval, corresponding with the $a^4\Pi_u$ ionic state, is shown in panel (d) of Fig. 3. Here the angular distribution features an emission pattern with a shallow minimum at $\pi/2$ and maximum intensity along the VUV field, exhibiting characteristics reminiscent of a p-wave, which is also reflected in the positive value of β_2 and small value of β_4 displayed in Table I.

The photoelectron angular distributions for the 4.20–5.50 eV, 5.50–6.20 eV and 5.50–7.00 eV intervals, associated with the $X^2\Pi_g$ ionic state, are displayed in panels (e), (f) and (g) of Fig. 3. The angular distributions exhibit a d-wave character, with peak intensity near $\pi/4$ and $3\pi/4$, and minima near 0, $\pi/2$, and π, also established by the calculated and fitted anisotropy parameters shown in Table I, with appreciably positive and negative values of β_2 and β_4, respectively. Despite the presence of the $(3\sigma_g)^{-1}n\sigma_g$ and $(3\sigma_g)^{-1}n\pi_g$ series of dipole-forbidden autoionizing states converging to the $B^2\Sigma_g^-$ ionic state (see Refs.[17,47]), which are known to play a crucial role in facilitating ion-pair formation at the two-photon energy used in the present study[17], the β parameters do not experience a significant change when comparing the two integration regions. This contrasts with our previous results on non-resonant two-photon single ionization of N_2[43], where a strong variation in the angular distributions, associated with different ionic states, was clearly observed with minor changes in the photoelectron kinetic energy. The rapid variations in the electron emission patterns were attributed to the excitation and decay of dipole-forbidden autoionizing resonances of different total symmetry. Here this effect appears suppressed, potentially due to the ion-pair formation mech-

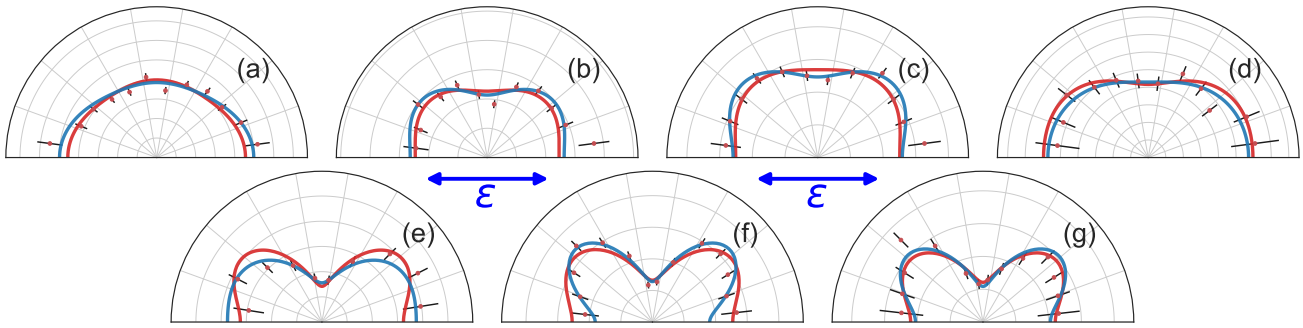

FIG. 3. Photoelectron angular distributions integrated over the kinetic energy intervals associated with the different ionic states $b^4\Sigma_g^-$: (a) 0.25–0.60 eV, $A^2\Pi_u$: (b) 0.80–1.20 eV, (c) 1.00–1.50 eV, $a^4\Pi_u$: (d) 2.00–2.50 eV, and $X^2\Pi_g$: (e) 4.20–5.50 eV, (f) 5.50–7.00 eV, and (g) 5.50–6.20 eV. Theoretical results are indicated by the solid red line, the experimental measurement indicated by the red points with black error bars (±1 standard deviation), and the fit to the experimental data shown as the solid blue line. The polarization vector ε of the VUV field is shown as the blue double sided arrows.

	State	Kinetic Energy (eV)	β_2 (theory)	β_4 (theory)	β_2 (exp)	β_4 (exp)
(a)	$b^4\Sigma_g^-$	0.25–0.60	0.069	0.061	0.16 ± 0.04	0.06 ± 0.06
(b)	$A^2\Pi_u$	0.80–1.20	0.109	-0.141	0.21 ± 0.05	-0.20 ± 0.07
(c)	$A^2\Pi_u$	1.00–1.50	0.007	-0.117	0.12 ± 0.05	-0.22 ± 0.07
(d)	$a^4\Pi_u$	2.00–2.50	0.278	-0.099	0.21 ± 0.07	-0.04 ± 0.10
(e)	$X^2\Pi_g$	4.20–5.50	0.633	-0.510	0.65 ± 0.08	-0.26 ± 0.11
(f)	$X^2\Pi_g$	5.50–7.00	0.536	-0.462	0.43 ± 0.05	-0.68 ± 0.06
(g)	$X^2\Pi_g$	5.50–6.20	0.511	-0.490	0.55 ± 0.07	-0.61 ± 0.10

TABLE I. Calculated and measured energy resolved photoelectron anisotropy β parameters corresponding to the photoelectron angular distributions shown in Fig. 3. The lettering used in Fig. 2 and Fig. 3 is shown in the leftmost column, for comparison. Note that all the theory values were obtained with the indicated photoelectron kinetic energy, but with same fixed bond length $R = 2.30$ a_0 so that, in particular, the value for the (e) energy interval does not include any possible changes from different geometries that this feature represents. The errors on the experimental β parameters are for ±1 standard deviation and were determined via statistical bootstrapping.

anism outcompeting autoionization[17].

V. DISCUSSION

The agreement between experiment and theory is good, and a few conclusions can be drawn from this result. First, as the initial photon absorption is near resonance with the $B^3\Sigma_u^-$ and $E^3\Sigma_u^-$ states [see Fig. 1(a)], and since the majority of the dipole coupling strength is for parallel transitions [see Fig. 1(b)], the inclusion of only two intermediate states in the calculations is adequate to accurately describe the photoionization processes and reproduce the experimental results. Hence, non-resonant two-photon transitions contribute negligibly to the measurement, and the intermediate electronic wavepacket is primarily composed of the superposition of the $B^3\Sigma_u^-$ and $E^3\Sigma_u^-$ states. It should be noted that, although only parallel transitions to the two $^3\Sigma_u^-$ intermediate states are considered in the first photoabsorption step, a $\cos^2(\phi)$ distribution of molecular orientations around the light polarization vector are excited, where ϕ is the angle between the internuclear axis and the light polarization vector ϵ, enabling perpendicular final state transitions.

Second, we note that for the $X^2\Pi_g$ ionic state, the one-photon Franck-Condon factors are similar in shape to the measured two-photon electron kinetic energy spectrum. This indicates that the ground state wavepacket is largely preserved, i.e. its distribution roughly maintained, on the intermediate electronic states as it transitions through them preceding ionization. This suggests that our measurement is mostly sensitive to early time dynamics on the intermediate states before the wavepacket can move or spread significantly. This enables the inclusion of only a single internuclear separation in the calculations in order to accurately reproduce the measured angular distributions, i.e. the role of nuclear motion can be ignored.

However, the signature of wavepacket motion and dissociation on the intermediate electronic states can still be observed in the weak photoelectron signal that lies between roughly 4.2–5.5 eV (see Fig. 2). As the wavepacket

dissociates, its binding energy increases and thus the photoelectron kinetic energy decreases. In the case of ionization to the $X^2\Pi_g$ ionic state, this causes the photoelectron kinetic energy to drop below the primary peak associated with the $X^2\Pi_g$ state, which is captured by the analyzed 4.2–5.5 eV region. The measured angular distribution associated with this region is shown in Fig. 3(e) and appears similar to that associated with the $X^2\Pi_g$ state, seen in Fig. 3(f) and (g), which indicates that these photoelectrons emerge from ionization to the ground state of the cation after the wavepacket exits the Franck-Condon region and begins to undergo dissociation. While our measurement primarily probes early times before the wavepacket can undergo significant motion, it still exhibits sensitivity to dissociation.

Last, as seen in Fig. 1(b) and discussed in section III, in the adiabatic representation, the Rydberg-valence mixed $B^3\Sigma_u^-$ and $E^3\Sigma_u^-$ states trade oscillator strength as the bond length varies, where summing their dipole couplings results in a relatively flat transition dipole moment across a range of internuclear separations, extending beyond the Franck-Condon region. We note that although these summed dipole couplings exhibit a slight decrease with increasing R, the variation in the coupling strength of the sum is significantly less than the variation in either of the two individual states. Both of these states possess the same symmetry, however, the two vary oppositely in their electronic character with bond length. It can be seen in Fig. 1(b) that at smaller internuclear separations, the $E^3\Sigma_u^-$ state possesses stronger dipole coupling with the ground electronic state, where the electronic character of the excited state is valence-like. Similarly, at larger internuclear distances, the $B^3\Sigma_u^-$ state possesses stronger dipole coupling, where its electronic character is also valence-like. This results in dominantly valence-character wavepackets forming regardless of the internuclear separation, with minimal Rydberg-character contribution to the ionization dynamics.

For photoionization to the $X^2\Pi_g$ state, the photoelectron angular distributions seen in Fig. 3(e), (f) and (g) do not appear diffuse and Rydberg-like, but are instead structured and exhibit a d-wave pattern, indicative of valence-character. This is true for both the primary photoelectron peak associated with the $X^2\Pi_g$ state, which corresponds to equilibrium internuclear distances, as well as the low energy shoulder that arises from dissocation, which corresponds to larger atomic separations, indicating valence-character at both small and large R.

VI. CONCLUSION

We have presented energy- and angle-resolved experimental and theoretical results on the photoionization dynamics of O_2, analyzing ionic-state-selective photoelectron angular distributions following near-resonant one-color two-photon single ionization of the neutral molecular ground state using coincidence 3-D momentum imaging and intense 9.3 eV femtosecond pulses produced via 400 nm driven HHG. We find agreement between experiment and theory, which indicates the involvement of a valence-Rydberg superposition of intermediate electronic states, and that non-resonant contributions are insignificant.

From the comparison of the experimental and theoretical angular distributions and asymmetry parameters, we conclude that wavepacket motion on the intermediate states does not significantly contribute to the measured two-photon ionization dynamics, although our measurement does demonstrate sensitivity to changes in internuclear distance. A superposition of the $B^3\Sigma_u^-$ and $E^3\Sigma_u^-$ states is created by photoexcitation with a 9.3 eV VUV photon, which is then probed by a second 9.3 eV photon from within the same pulse envelope. The contribution from each component of the superposition changes with bond length, which results in a valence-character wavepacket being created irrespective of internuclear distance. In particular, at shorter bond lengths, the dipole coupling between the ground state and $E^3\Sigma_u^-$ state is dominant, where this state shows strong valence-character, while at larger bond lengths, the $B^3\Sigma_u^-$ state dipole coupling is dominant, where this state also possesses strong valence-character. As the relative composition of the superposition varies with bond length, the electronic character remains valence-like. In this sense, the diabatic representation constructed from the $B^3\Sigma_u^-$ and $E^3\Sigma_u^-$ states is simpler and more effective for understanding this experiment than the adiabatic representation, since in the diabatic representation the majority of the oscillator strength is carried by only the valence-character diabat in the expression for both intermediate states. This results in the measured photoelectron angular distributions not exhibiting strong dependence on the bond length, allowing nuclear motion to be neglected in the calculations. The calculated angular distributions show very good agreement with their measured counterparts for all four ionic final states of O_2^+ using exclusively the single internuclear distance of R = 2.3 bohr.

The one-color two-photon single ionization scheme likely loses sizable yield to prompt dissociation of the excited oxygen molecule on the $B^3\Sigma_u^-$ state. If the dissociating molecule does not absorb the second 9.3 eV photon shortly after the first, the wavepacket will exit the ionization window and those events dissociate into neutral oxygen fragments, depleting the excited state target. However, this reaction channel is not part of the O_2^+ cation-electron coincidence detection scheme and does not affect or pollute the measured electron angular distributions - it only reduces the two-photon ionization and data acquisition rate.

Further investigation on the dependence of the photoelectron angular distributions on R is needed to fully evaluate the role of wavepacket motion in influencing the measured two-photon ionization dynamics. Any deviations between the experimental and theoretical angular distributions and asymmetry parameters are likely due

to the choice of the internuclear distances, which was set to the equilibrium distance of the neutral molecule in the calculation and yielded very good agreement. Future experiments could explore the avoided crossing with slightly lower and higher photon energies, sampling a larger fraction of the internuclear distances in the Franck-Condon region and changing the relative composition of the electronic wavepacket that is prepared.

VII. ACKNOWLEDGMENTS

Work at LBNL was supported by the U.S. Department of Energy Office of Basic Energy Sciences, Division of Chemical Sciences, Biosciences, and Geosciences under contract No. DE-AC02-05CH11231 and used resources of the National Energy Research Computing Center, a United States Department of Energy (US DOE) Office of Science User Facility supported by the Office of Science of the DOE under Contract No. DE-AC02-05CH11231 using NERSC award BES-ERCAP-0020143 (theory) and BES-ERCAP-0019776 (experiment), and the Lawrencium computational cluster resource provided by the IT Division at the Lawrence Berkeley National Laboratory. We thank the RoentDek Handels GmbH for longtime support with hardware and software.

VIII. DATA AVAILABILITY

The data supporting the findings of this study are available from the corresponding authors upon request.

[1]F. Holzmeier, R. Y. Bello, M. Hervé, A. Achner, T. M. Baumann, M. Meyer, P. Finetti, M. Di Fraia, D. Gauthier, E. Roussel, O. Plekan, R. Richter, K. C. Prince, C. Callegari, H. Bachau, A. Palacios, F. Martín, and D. Dowek. Control of H_2 dissociative ionization in the nonlinear regime using vacuum ultraviolet free-electron laser pulses. *Phys. Rev. Lett.*, 121:103002, Sep 2018. doi:10.1103/PhysRevLett.121.103002.

[2]P. Lambropoulos. Topics on multiphoton processes in atoms. volume 12 of *Advances in Atomic and Molecular Physics*, pages 87–164. Academic Press, 1976. doi:10.1016/S0065-2199(08)60043-3.

[3]A.T. Georges and P. Lambropoulos. Aspects of resonant multiphoton processes. volume 54 of *Advances in Electronics and Electron Physics*, pages 191–240. Academic Press, 1980. doi:10.1016/S0065-2539(08)60099-2.

[4]Amalia Apalategui, Alejandro Saenz, and P Lambropoulos. Effect of vibration and internuclear axis orientation on multiphoton ionization of H_2^+. *Journal of Physics B: Atomic, Molecular and Optical Physics*, 33(14):2791–2807, jul 2000. doi:10.1088/0953-4075/33/14/316.

[5]E Karule. Analytical continuation of the transition matrix elements and multiphoton above-threshold ionisation of atomic hydrogen. *Journal of Physics B: Atomic, Molecular and Optical Physics*, 21(11):1997–2014, jun 1988. doi:10.1088/0953-4075/21/11/015.

[6]E Karule and B Moine. The general expression for the transition amplitude of two-photon ionization of atomic hydrogen. *Journal of Physics B: Atomic, Molecular and Optical Physics*, 36(10):1963–1969, may 2003. doi:10.1088/0953-4075/36/10/307.

[7]J. Wang, D.G. McCoy, A.J. Blake, and L. Torop. Effects of the close approach of potential curves in photoabsorption by diatomic molecules—II. temperature dependence of the O_2 cross section in the region 130–160 nm. *Journal of Quantitative Spectroscopy and Radiative Transfer*, 38(1):19 – 27, 1987. ISSN 0022-4073. doi:10.1016/0022-4073(87)90106-3.

[8]N. Balakrishnan, M. J. Jamieson, A. Dalgarno, Y. Li, and R. J. Buenker. Time-dependent quantum mechanical study of photodissociation of molecular oxygen in the Schumann–Runge continuum. *The Journal of Chemical Physics*, 112(3):1255–1259, 2000. doi:10.1063/1.480657.

[9]Robert J Buenker and Sigrid D Peyerimhoff. Ab initio study of the mixing of valence and Rydberg states in O_2: CI potential curves for the $^3\Sigma_u^-$, $^3\Delta_u$ and $^3\Pi_u$ states. *Chemical Physics Letters*, 34(2):225–231, 1975. doi:10.1016/0009-2614(75)85260-2.

[10]L Torop, DG McCoy, AJ Blake, Jingbo Wang, and T Scholz. Effects of the close approach of potential curves in photoabsorption by diatomic molecules—I. theory and computational procedures. *Journal of Quantitative Spectroscopy and Radiative Transfer*, 38 (1):9–18, 1987. doi:10.1016/0022-4073(87)90105-1.

[11]AC Allison, SL Guberman, and A Dalgarno. A model of the Schumann-Runge continuum of O_2. *Journal of Geophysical Research: Space Physics*, 91(A9):10193–10198, 1986. doi:10.1029/JA091iA09p10193.

[12]Megumu Yoshimine, Kiyoshi Tanaka, Hiroshi Tatewaki, Sigeru Obara, Fukashi Sasaki, and Kimio Ohno. The second $^3\Sigma_u^-$ state of O_2. *The Journal of Chemical Physics*, 64(5):2254–2255, 1976. doi:10.1063/1.432452.

[13]Robert J Buenker, Sigrid D Peyerimhoff, and Miljenko Perić. Ab initio vibrational analysis of the Schumann—Runge bands and the neighboring absorption region of molecular oxygen. *Chemical Physics Letters*, 42(2):383–389, 1976. doi:10.1016/0009-2614(76)80391-0.

[14]Hiroshi Tatewaki, Kiyoshi Tanaka, Fukashi Sasaki, Shigeru Obara, Kimio Ohno, and Megumu Yoshimine. Configuration-interaction study of lower excited states of O_2: Valence and Rydberg characters of the two lowest $^3\Sigma_u^-$ states. *International Journal of Quantum Chemistry*, 15(5):533–545, 1979. doi:10.1002/qua.560150509.

[15]B. R. Lewis, J. P. England, S. T. Gibson, M. J. Brunger, and M. Allan. Electron energy-loss spectra of coupled electronic states: Effects of Rydberg-valence interactions in O_2. *Phys. Rev. A*, 63:022707, Jan 2001. doi:10.1103/PhysRevA.63.022707.

[16]B. R. Lewis, S. T. Gibson, S. S. Banerjee, and H. Lefebvre-Brion. Relations between Rydberg-valence interactions in the O_2 molecule. *The Journal of Chemical Physics*, 113(6):2214–2223, 2000. doi:10.1063/1.482035.

[17]Kirk A. Larsen, Robert R. Lucchese, Daniel S. Slaughter, and Thorsten Weber. Distinguishing resonance symmetries with energy-resolved photoion angular distributions from ion-pair formation in O_2 following two-photon absorption of a 9.3 eV femtosecond pulse. *The Journal of Chemical Physics*, 153(2):021103, 2020. doi:10.1063/5.0013485.

[18]R. Dörner, V. Mergel, O. Jagutzki, L. Spielberger, J. Ullrich, R. Moshammer, and H. Schmidt-Böcking. Cold Target Recoil Ion Momentum Spectroscopy: a 'momentum microscope' to view atomic collision dynamics. *Physics Reports*, 330(2-3):95–192, June 2000. ISSN 0370-1573. doi:10.1016/S0370-1573(99)00109-X.

[19]J Ullrich, R Moshammer, A Dorn, R Dörner, L Ph H Schmidt, and H Schmidt-Böcking. Recoil-ion and electron momentum spectroscopy: reaction-microscopes. *Reports on Progress in Physics*, 66(9):1463–1545, aug 2003. doi:10.1088/0034-4885/66/9/203.

[20]T. Jahnke, Th. Weber, T. Osipov, A.L. Landers, O. Jagutzki, L.Ph.H. Schmidt, C.L. Cocke, M.H. Prior, H. Schmidt-Böcking, and R. Dörner. Multicoincidence studies of photo and Auger electrons from fixed-in-space molecules using the COLTRIMS technique. *Journal of Electron Spectroscopy and Related Phenomena*, 141(2):229–238, 2004. ISSN 0368-2048. doi:10.1016/j.elspec.2004.06.010. Frontiers of Coincidence Experiments.

[21]F. P. Sturm, T. W. Wright, D. Ray, I. Zalyubovskaya, N. Shivaram, D. S. Slaughter, P. Ranitovic, A. Belkacem, and Th. Weber. Time resolved 3D momentum imaging of ultrafast dynamics by coherent VUV-XUV radiation. *Review of Scientific Instruments*, 87(6):063110, 2016. doi:10.1063/1.4953441.

[22]O. Jagutzki, A. Cerezo, A. Czasch, R. Dorner, M. Hattas, Min Huang, V. Mergel, U. Spillmann, K. Ullmann-Pfleger, T. Weber, H. Schmidt-Bocking, and G.D.W. Smith. Multiple hit readout of a microchannel plate detector with a three-layer delay-line anode. *IEEE Transactions on Nuclear Science*, 49(5):2477–2483, 2002. doi:10.1109/TNS.2002.803889.

[23]T. K. Allison, J. van Tilborg, T. W. Wright, M. P. Hertlein, R. W. Falcone, and A. Belkacem. Separation of high order harmonics with fluoride windows. *Opt. Express*, 17(11):8941–8946, May 2009. doi:10.1364/OE.17.008941.

[24]H. H. Li. Refractive index of alkaline earth halides and its wavelength and temperature derivatives. *Journal of Physical and Chemical Reference Data*, 9(1):161–290, 1980. doi: 10.1063/1.555616.

[25]Taro Sekikawa, Tomotaka Katsura, Satoshi Miura, and Shuntaro Watanabe. Measurement of the intensity-dependent atomic dipole phase of a high harmonic by frequency-resolved optical gating. *Phys. Rev. Lett.*, 88:193902, Apr 2002. doi: 10.1103/PhysRevLett.88.193902.

[26]Taro Sekikawa, Tomoki Ohno, Tomohiro Yamazaki, Yasuo Nabekawa, and Shuntaro Watanabe. Pulse compression of a high-order harmonic by compensating the atomic dipole phase. *Phys. Rev. Lett.*, 83:2564–2567, Sep 1999. doi: 10.1103/PhysRevLett.83.2564.

[27]K. A. Larsen, J. P. Cryan, N. Shivaram, E. G. Champenois, T. W. Wright, D. Ray, O. Kostko, M. Ahmed, A. Belkacem, and D. S. Slaughter. VUV and XUV reflectance of optically coated mirrors for selection of high harmonics. *Opt. Express*, 24(16): 18209–18216, Aug 2016. doi:10.1364/OE.24.018209.

[28]Kirk A. Larsen, Daniel S. Slaughter, and Thorsten Weber. Angle-resolved nonresonant two-photon single ionization of argon using 9.3-eV photons produced via high-order harmonic generation. *Phys. Rev. A*, 101:061402, Jun 2020. doi: 10.1103/PhysRevA.101.061402.

[29]Richard N. Dixon. Recoil anisotropy following multiphoton dissociation via near-resonant intermediate states. *The Journal of Chemical Physics*, 122(19):194302, 2005. doi:10.1063/1.1896951.

[30]R.N. Dixon, J.M. Bayley, and M.N.R. Ashfold. The rotational structure of three-photon resonances of polyatomic molecules. *Chemical Physics*, 84(1):21 – 34, 1984. ISSN 0301-0104. doi: 10.1016/0301-0104(84)80003-8.

[31]George C. Nieman. Vibronic intensities and rotational line strength factors for the three-photon absorption spectrum of ammonia. *The Journal of Chemical Physics*, 75(2):584–595, 1981. doi:10.1063/1.442074.

[32]R.G. Bray and R.M. Hochstrasser. Two-photon absorption by rotating diatomic molecules. *Molecular Physics*, 31(4):1199–1211, 1976. doi:10.1080/00268977600100931.

[33]David L. Andrews. The theory of double-beam three-photon absorption. *The Journal of Chemical Physics*, 77(6):2831–2835, 1982. doi:10.1063/1.444174.

[34]Warner L. Peticolas, Robert Norris, and Klaus E. Rieckhoff. Polarization effects in the two-photon excitation of anthracene fluorescence. *The Journal of Chemical Physics*, 42(12):4164–4169, 1965. doi:10.1063/1.1695913.

[35]Hans-Joachim Werner, Peter J. Knowles, Gerald Knizia, Frederick R. Manby, and Martin Schütz. MOLPRO: a general-purpose quantum chemistry program package. *WIREs Computational Molecular Science*, 2(2):242–253, 2012. doi:10.1002/wcms.82.

[36]H.-J. Werner, P. J. Knowles, G. Knizia, F. R. Manby, M. Schütz, P. Celani, T. Korona, R. Lindh, A. Mitrushenkov, G. Rauhut, K. R. Shamasundar, T. B. Adler, R. D. Amos, A. Bernhardsson, A. Berning, D. L. Cooper, M. J. O. Deegan, A. J. Dobbyn, F. Eckert, E. Goll, C. Hampel, A. Hesselmann, G. Hetzer, T. Hrenar, G. Jansen, C. Köppl, Y. Liu, A. W. Lloyd, R. A. Mata, A. J. May, S. J. McNicholas, W. Meyer, M. E. Mura, A. Nicklass, D. P. O'Neill, P. Palmieri, D. Peng, K. Pflüger, R. Pitzer, M. Reiher, T. Shiozaki, H. Stoll, A. J. Stone, R. Tarroni, T. Thorsteinsson, and M. Wang. MOLPRO, version 2015.1, a package of ab initio programs, 2015.

[37]Thom H. Dunning. Gaussian basis sets for use in correlated molecular calculations. I. The atoms boron through neon and hydrogen. *The Journal of Chemical Physics*, 90(2):1007–1023, 1989. doi:10.1063/1.456153.

[38]Rick A. Kendall, Thom H. Dunning, and Robert J. Harrison. Electron affinities of the first-row atoms revisited. Systematic basis sets and wave functions. *The Journal of Chemical Physics*, 96(9):6796–6806, 1992. doi:10.1063/1.462569.

[39]K Kaufmann, W Baumeister, and M Jungen. Universal Gaussian basis sets for an optimum representation of Rydberg and continuum wavefunctions. *Journal of Physics B: Atomic, Molecular and Optical Physics*, 22(14):2223–2240, jul 1989. doi: 10.1088/0953-4075/22/14/007.

[40]R. E. Stratmann and Robert R. Lucchese. A graphical unitary group approach to study multiplet specific multichannel electron correlation effects in the photoionization of O_2. *The Journal of Chemical Physics*, 102(21):8493–8505, 1995. doi: 10.1063/1.468841.

[41]R. E. Stratmann, Robert W. Zurales, and Robert R. Lucchese. Multiplet-specific multichannel electron-correlation effects in the photoionization of NO. *The Journal of Chemical Physics*, 104 (22):8989–9000, 1996. doi:10.1063/1.471632.

[42]Roger Y. Bello, Robert R. Lucchese, Thomas N. Rescigno, and C. William McCurdy. Correlated variational treatment of ionization coupled to nuclear motion: Ultrafast pump and ionizing probe of electronic and nuclear dynamics in LiH. *Phys. Rev. Research*, 3:013228, Mar 2021. doi: 10.1103/PhysRevResearch.3.013228.

[43]Kirk A. Larsen, Roger Y. Bello, Robert R. Lucchese, Thomas N. Rescigno, C. William McCurdy, Daniel S. Slaughter, and Thorsten Weber. Role of dipole-forbidden autoionizing resonances in nonresonant one-color two-photon single ionization of N_2. *Phys. Rev. A*, 102:063118, Dec 2020. doi: 10.1103/PhysRevA.102.063118.

[44]P. Baltzer, B. Wannberg, L. Karlsson, M. Carlsson Göthe, and M. Larsson. High-resolution inner-valence UV photoelectron spectra of the O_2 molecule and configuration-interaction calculations of $^2\Pi_u$ states between 20 and 26 eV. *Phys. Rev. A*, 45: 4374–4384, Apr 1992. doi:10.1103/PhysRevA.45.4374.

[45]O Edqvist, E Lindholm, L E Selin, and L Åsbrink. On the photoelectron spectrum of O_2. *Physica Scripta*, 1(1):25–30, jan 1970. doi:10.1088/0031-8949/1/1/004.

[46]Bradley Efron. *Bootstrap Methods: Another Look at the Jackknife*, pages 569–593. Springer New York, New York, NY, 1992. ISBN 978-1-4612-4380-9. doi:10.1007/978-1-4612-4380-9˙41.

[47]Sonia Marggi Poullain, Markus Klinker, Jesús González-Vázquez, and Fernando Martín. Resonant photoionization of O_2 up to the fourth ionization threshold. *Phys. Chem. Chem. Phys.*, 21:16497–16504, 2019. doi:10.1039/C9CP02150G.